BATTERIES & SUPERCAPS

A Gas Diffusion Layer Impregnated with Mn_3O_4-Decorated N-Doped Carbon Nanotubes for the Oxygen Reduction Reaction in Zinc-Air Batteries

Drew Aasen,[a] Michael Clark,[a] and Douglas G. Ivey*[a]

Mn_3O_4-decorated N-CNTs are synthesized and impregnated into porous carbon paper (gas diffusion layer or GDL) to form a composite catalyst-GDL material in a simple and novel one-pot process. The impregnated electrode features high active surface area, improved discharge performance, and reduced vulnerability to flooding when compared with other electrode preparation techniques for similar catalysts. Electrochemical and battery testing show catalytic activity and a maximum discharge potential superior to other CNT supported Mn_3O_4 catalysts, and comparable to commercially used Pt–Ru (1.21 V at 20 mA cm^{-2}). The composite is cycled at 10 mA cm^{-2} and 20 mA cm^{-2} as a bifunctional catalyst and as an oxygen reduction reaction (ORR) exclusive catalyst, respectively. Discharge performance is stable over 200 cycles at 20 mA cm^{-2} when used exclusively for ORR with a discharge-charge efficiency superior to Pt–Ru when coupled with electrodeposited Co–Fe as the OER catalyst (efficiency of 59% after cycling).

1. Introduction

Zn-air batteries (ZABs) have garnered recent interest for energy storage battery technology as they have high theoretical energy densities, minimal safety concerns, and low environmental impact relative to other battery types.[1,2] However, the slow kinetics of the oxygen reduction and oxygen evolution reactions (ORR and OER) result in energy losses and comparably low efficiencies.[1,3,4] Commonly, precious metals such as Pt, Ru, Ir, and their oxides have been used as catalysts to enhance the kinetics of the ORR and OER but suffer from high cost and poor stability during cycling.[5,6] Therefore, it is desirable to find an economical alternative to precious metal catalysts to enhance the practicality of ZABs.

Extensive work has been conducted in developing transition metals and their oxides into effective catalysts for ORR and OER.[7–9] Various manganese oxides (MnO_x) in particular have attracted a great deal of interest as cost effective catalysts for ORR due to the abundance of Mn and Mn oxide's stability in alkaline solutions.[4,10] However, their use in ZABs has been limited due to their poor electrical conductivity and poor stability during the harsh oxidizing conditions of OER.[3,10,11] Additionally, the electro-active surface area and number of catalytically active sites of MnO_x are relatively low.[12] A number of strategies have been applied to combat these issues, namely using carbon based supports as well as various nanocarbons such as carbon nanotubes (CNTs), graphene, and carbon black to make composite catalyst materials.[10,13] The use of non-metal

(B, S, N, O, P), doped nanocarbons has been shown to increase the number of active sites in the catalyst material when compared with un-doped nanocarbon catalysts.[14–16] Nitrogen is the most common non-metal dopant in nanocarbon structures due to the similarity in atomic size of N and C, coupled with an increase in activity towards ORR.[17,18] By combining N-doped nanocarbons and metals/metal oxides, the catalyst performance can be greatly enhanced due to nitrogen-carbon-metal (N–C–M) synergistic effects.[13,19] For instance, Mn_3O_4 quantum dots were anchored to partially exfoliated, N-doped multiwalled CNTs by Huang et al., showing good activity towards ORR and good stability in a mechanically rechargeable Zn-air battery.[20] Similarly, Mn_3O_4 particles were synthesized onto CNTs and were treated with oxygen plasma to achieve Mn_3O_4/O-CNTs and were shown to have good stability during cycling.[21] Thus, combining MnO_x and N-CNTs is predicted to have high performance towards ORR and better stability than MnO_x alone. However, synthesis of metal oxides supported on doped nano-carbon materials is often quite complex and may require acid or mechanical treatments to functionalize the carbon materials prior to doping and synthesis..[17,20–22] Chemical vapour deposition and hydrothermal methods, among various other techniques, are commonly employed to achieve the desired catalysts.[17,23,24]

Many strategies have improved the intrinsic activity of the catalysts; however, an issue is still faced during electrode preparation. Poor adherence of the catalyst layer to the gas diffusion layer (GDL) greatly increases the contact resistance and results in reduced electrochemical performance of the battery.[1,4,25] Often, the electrode is prepared by spraying a catalyst ink onto the GDL surface or mixing catalyst powders into a slurry and applying the slurry onto the GDL.[9,25,26] Binders, such as Nafion and PTFE, are added to the ink/slurry to improve adhesion to the electrode and minimize delamination, although many binders are not stable in the operating conditions of the

[a] D. Aasen, M. Clark, Prof. D. G. Ivey
Department of Chemical and Materials Engineering,
University of Alberta,
Edmonton Alberta, Canada T6G 1H9
E-mail: divey@ualberta.ca

battery.[1,4,25] Electrodeposition has been explored as a binder-free solution to this issue and provides better adherence to the electrode.[3,27,28] All three methods still struggle with the issue of flooding as performance is lost once the electrolyte passes through the surface-bound catalyst layer.[1,4] To mitigate the issue of flooding and preserve the interface between the air, electrolyte, and catalysts, a composite air electrode with catalysts dispersed through its porosity is ideal. Furthermore, achieving such an electrode by relatively simple means while maintaining competitive electrochemical performance is desired. Impregnating the microporous layer of the GDL with nanosized catalysts is a logical answer to this proposition, as it is a potentially simple and cost-effective method to fabricate a composite electrode without the need for excessive materials or expensive equipment. Moreover, impregnating the micro-porous layer of the GDL would increase the exposed and active surface areas of the electrode, thus improving battery perform-ance. For instance, MnO_2 was grown directly on carbon paper by Sumboja et al. via an immersion process followed by heat treatment for 24 h.[29] The direct-growth of MnO_2 showed superior performance to an applied MnO_2 powder due to better adhesion, a maintained three-phase boundary, and better contact with the electrode which facilitated charge transfer.[29] Similarly, Li et al. soaked carbon cloth in an ink consisting of

Mn_3O_4/O-CNTs.[21] However, the carbon cloth was then applied to the surface of the GDL to be used as the air electrode resulting in a surface-bound catalyst layer. To the best of our knowledge, impregnation has not otherwise been explored as a means of electrode preparation for ZABs, specifically with regards to CNT supported catalysts.

In the current study, nanoparticle Mn_3O_4-decorated N-CNTs are synthesized and impregnated into the GDL simultaneously in a simple, one-pot synthesis process using only the catalyst precursor solution and a piece of GDL. Mn_3O_4-decorated N-CNTs enter the microporous layer of the GDL, allowing continuous contact between the air and electrolyte as the electrolyte begins to enter the electrode. Additionally, the high surface areas of the Mn_3O_4 nanoparticles, coupled with the increased active sites, electrical conductivity, and surface area of the N-CNTs, can provide performance superior to Mn_3O_4/N-CNT catalysts previously reported in the literature, particularly for ORR. The synthesis and electrode preparation processes are done together and may be repeated to fabricate multiple air electrodes from a single solution. The result is a simple and cost-effective method of preparing a high performing air electrode for ZABs.
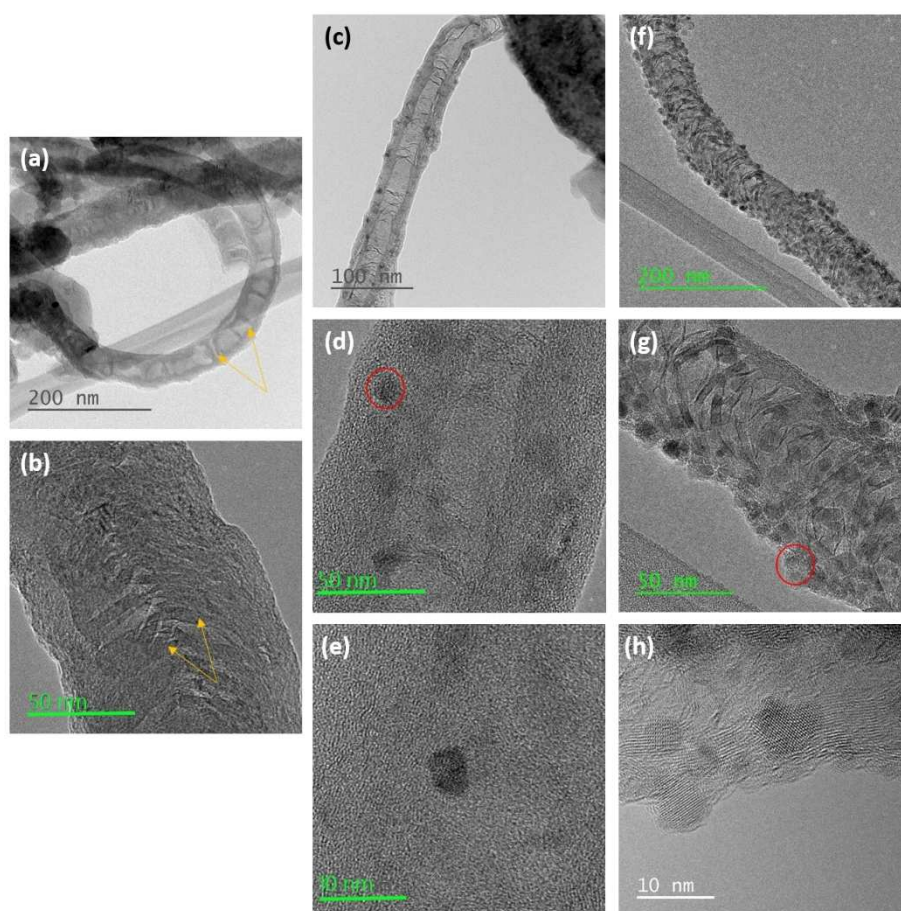

Figure 1. TEM bright field (BF) micrographs of a), b) N-CNTs; c)–e) as prepared Mn_3O_4/N-CNT/GDL, and f)–h) annealed Mn_3O_4/N-CNT/GDL. Arrows mark nitrogen-induced defects in the CNT walls and circles highlight Mn oxide particles in the Mn_3O_4/N-CNT/GDL samples.

2. Results and Discussion

Figure 1 shows TEM images of N-CNTs and synthesized Mn oxide-decorated N-CNTs (Mn_3O_4/N-CNT/GDL samples) in both the as prepared (Figure 1c-1e) and annealed (Figure 1f-1 g) conditions. The N-CNTs clearly show the bamboo-like structure expected from the nitrogen doping (Figure 1a and 1b).[17] Comparison of the N-CNTs with the Mn_3O_4/N-CNTs shows that Mn oxide particles preferentially nucleate along the nitrogen induced defects within the CNT walls. TEM analysis of Mn_3O_4/CNT samples (no nitrogen doping) confirms the importance of nitrogen for Mn oxide particle attachment to the nanotubes (Figure S2). Clusters of nanoparticles (10–20 nm in size) form and intertwine with the undoped CNTs; however, HRTEM imaging of the CNTs shows no evidence of MnO_x particles on the surface (Figure S2a–S2c; also confirmed by EDX mapping). Therefore, Mn oxide particles do not decorate the CNTs without N doping. Nucleation of the Mn oxide particles on N-CNTs occurs during the mixing process (as indicated by the particles in Figure 1c-1 h), where the Mn^{2+} ions are attracted to the negative dipole created by the slight difference in electronegativity caused by the nitrogen heteroatoms.[17] Additionally, the Mn oxide particles nucleate on the defects in order to reduce the overall energy of the material, resulting in two driving forces for the formation of the Mn oxide particles. Examination of the particles, both as fabricated and annealed, at higher magnification (Figure 1e and 1 h), shows that they are clearly crystalline and ~5–10 nm in size.

EDX maps from one of the nanotubes decorated with Mn oxide (annealed condition) are shown in Figure 2a. The O and Mn signals overlap, which clearly indicates the Mn particles are oxidized. EDX maps taken from the as fabricated sample (not shown here) are similar, which means that Mn oxide forms prior to annealing. EDX maps from the Mn_3O_4/CNT samples also show overlap between the Mn and O signals (Figure S2f). However, Mn and O signals are only observed over the particle clusters and not on the CNTs. Nickel particles were also detected through EDX analysis and these are remnants of the synthesis of CNTs and N-CNTs, during which Ni acts as a catalyst.[17][18] Selected area diffraction (SAD) patterns of the Mn oxide-decorated N-CNTs are shown in Figure 2b (as fabricated) and 2c (annealed) and are evaluated in Table 1. The pattern in Figure 2b shows 2 sets of rings; the faint, continuous rings are from carbon (N-CNTs), while the spotty, discontinuous rings are from the Mn oxide. The Mn oxide rings for the as fabricated sample can be indexed to Mn_3O_4, to both the cubic spinel ($a = 0.842$ nm – PDF #13-0162) and tetragonal spinel (hausmannite, with $a = 0.5762$ nm and $c = 0.947$ nm – PDF #01-071-6262) structures. The SAD pattern from the annealed sample (Figure 2c) also shows two sets of rings, corresponding to carbon from the N-CNTs and Mn oxide. The Mn oxide pattern can also be indexed to both cubic and tetragonal Mn_3O_4. Similarly, the Mn oxide in the undoped CNT samples was also identified as Mn_3O_4 (SAD pattern in Figure S2d). Based on the TEM diffraction data, conclusive identification of the form of Mn_3O_4 was not possible.
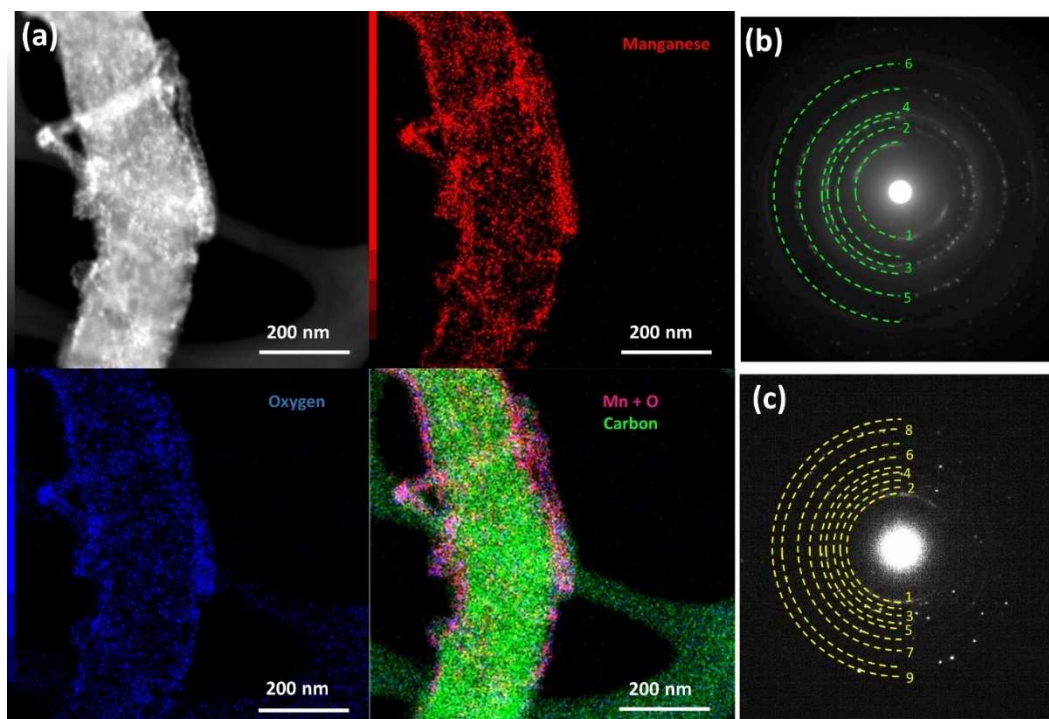

Figure 2. a) STEM high-angle annular dark field (HAADF) micrograph, EDX elemental maps, and EDX map overlay for Mn_3O_4/N-CNT/GDL in the annealed condition. In the EDX map overlay, the combined Mn (red) and O (blue) signals generate a pink color. b) SAD pattern obtained from as fabricated Mn_3O_4/N-CNT/GDL. c) SAD pattern obtained from annealed Mn_3O_4/N-CNT/GDL. Coloured and dashed lines are used to illustrate the rings on the diffraction patterns, while numbers are used to label each ring (b, c). Associated crystal structure information is presented in Table 1.

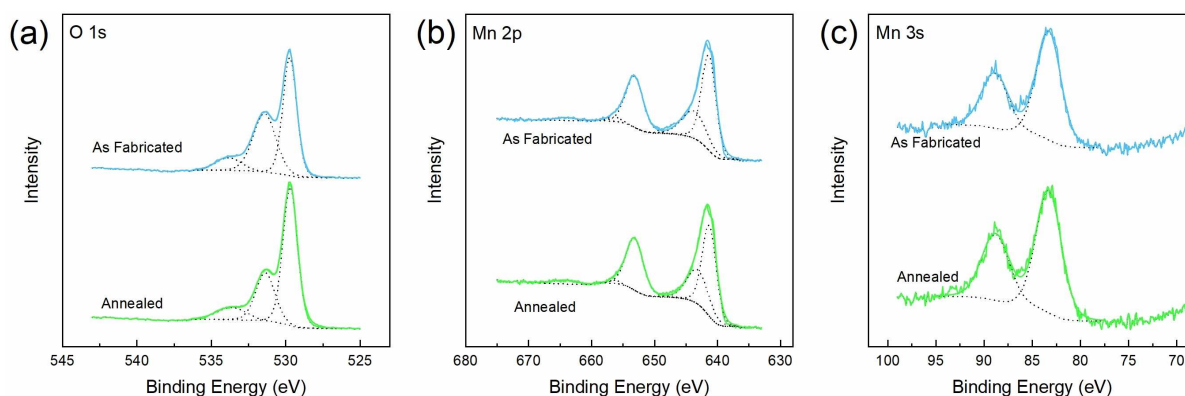**Table 1.** SAD pattern d-spacings and Miller indices for as-fabricated and annealed Mn₃O₄/N-CNT/GDL.

As-fabricated SAD (Figure 2b)				Annealed SAD (Figure 2c)			
Ring number	d spacing (Å)	Cubic $(h\,k\,l)$	Tetragonal $(h\,k\,l)$	Ring number	d Spacing (Å)	Cubic $(h\,k\,l)$	Tetragonal $(h\,k\,l)$
1	3.36[a]	–	–	1	3.38[a]	–	–
–	–	–	–	2	2.77	(2 2 0)	(1 0 3)
2	2.49	(3 1 1)	(2 1 1)	3	2.45	(2 2 2)	(2 0 2)
3	2.15	(4 0 0)	–	–	–	–	–
4	2.05[a]	–	–	4	2.03[a]	–	(2 2 0)
				5	2.01	–	(2 1 3)
–	–	–	–	6	1.77	(4 2 2)	(1 0 5)
–	–	–	–	7	1.74[a]	–	–
5	1.53	(4 4 0)	(2 2 4)	8	1.54	(4 4 0)	(2 2 4)
6	1.25	(5 3 3)	(4 2 2)	9	1.17	(4 4 4)	(0 0 8)

[a] Indicates carbon ring.

The as fabricated samples are coated with an organic film which contains Na, from the NaOH added during the mixing step. This layer makes imaging and EDX analysis in the TEM problematic, as a contamination layer builds up on the surface during exposure to the electron beam (Figure S3). The Na-containing film burns off during annealing, leaving the N-CNTs with embedded Mn₃O₄. Therefore, the main effect of annealing the sample is the removal of the Na-containing film and excess water.

The formation of Mn₃O₄ was confirmed using XPS (Figure 3 and Table 2). The valence of Mn is estimated using the Mn 2p and 3s peaks and the O 1s peak. Deconvolution of the O 1s peak (Figure 3a) yields three peaks which correspond to Mn−O−Mn bonds (529.3–530.0 eV), Mn−O−H bonds (530.5–531.5 eV), and H−O−H bonds (531.8–532.8 eV), respectively. The spectra are comparable to reports in literature for various Mn oxides.[30] The difference in the Mn−O−H and H−O−H peaks

between the as-fabricated and annealed samples is a result of the annealing process where excess water is evaporated. The Mn 2p peak (Figure 3b) for the as-fabricated and annealed samples can be deconvoluted into 2 major components which correspond to Mn $2p_{1/2}$ and Mn $2p_{3/2}$ with positions at approximately 653 eV and 641 eV, respectively. Three minor components are also present in the Mn 2p data. These components correspond to Mn^{2+} and Mn^{3+} which have been reported for MnO and Mn₂O₃ XPS data in the literature.[31] Using the areas under the peaks corresponding to Mn^{2+} and Mn^{3+}, the Mn valence of the samples can be estimated by use of a weighted average (Table 2).[32] The separation between the Mn−O−Mn component of the O 1s peak and the Mn $2p_{3/2}$ component from the deconvoluted Mn 2p peak has also been reported as a tool for determining Mn valence ($\Delta2p$–1s).[30] Additionally, Mn 3 s peak separation (Figure 3c) is often used as a factor in determining Mn valence.[30,31,33] The 3s peak splitting

Figure 3. XPS results for the as-fabricated and annealed Mn₃O₄/N-CNT/GDL samples. a) O 1s spectra, b) Mn 2p spectra, and c) Mn 3s spectra. Deconvolution of the peaks is represented by dashed lines.

Table 2. XPS data and Mn valence using Mn 2p, Mn 3s, and O1s peaks.

XPS Sample	Mn 2p 2+peak (eV)	3+peak (eV)	Mn 3s Peak 1 (eV)	Peak 2 (eV)	Δ3s (eV)	Mn valence (2p)	Mn valence (3s)	Δ2p-1s (eV)
As-fabricated	656.32	664.28	88.855	83.295	5.56	2.50	2.47	111.7
Annealed	656.25	664.48	88.787	83.294	5.49	2.64	2.58	111.6
Reference Mn₃O₄[30]	–	–	88.30–88.86	83.00–83.36	~5.5	~2.67		111.5–111.8

Table 3. EDX point analysis data for Mn$_3$O$_4$/GDL and Mn$_3$O$_4$/N-CNT/GDL samples presented in Figure 4.

Spectrum	Sample	C (wt%)	O (wt%)	F (wt%)	Ni (wt%)	Mn (wt%)	Figure
1	Mn$_3$O$_4$/GDL	90.8	1.9	7.3			4b
2	Mn$_3$O$_4$/GDL	12.9	26.1	19.7		40.4	4b
3	Mn$_3$O$_4$/N-CNT/GDL	33.8	17.9	13.3	4.7	30.3	4f

is a result of an exchange interaction between the 3s and 3d orbitals upon photoelectron ejection.[30] Therefore, wider peak splitting is observed for lower valence. From the Mn 3s splitting, Mn 2p data, and Δ2p–1s results, it can be confirmed that Mn$_3$O$_4$ is formed in both as-fabricated and annealed Mn$_3$O$_4$/N-CNT/GDL, since the estimated valence is close to the 2.67 value expected for Mn$_3$O$_4$ (Table 2).[30,31,33] These results corroborate the TEM diffraction results discussed above.

Mn$_3$O$_4$/GDL samples (no CNTs) were compared with Mn$_3$O$_4$/N-CNT/GDL samples (Figure 4). A dense Mn oxide film is visible in Figure 4a and 4b for the sample without CNTs, which suggests that individual nanoparticles are not achieved without the presence of N-CNTs. This is confirmed by the compositions obtained through EDX analysis (Table 3) and the lack of Mn on the GDL within the cracks of the Mn oxide film (Figure 4c). Cracking of the Mn oxide film is likely due to drying of the film during the annealing step. By contrast, Mn$_3$O$_4$ particles are visible on the N-CNTs for the Mn$_3$O$_4$/N-CNT/GDL sample in Figure 4f and no continuous Mn oxide film is visible in the lower magnification images (Figure 4d and 4e). Furthermore, Figure 4 shows Mn$_3$O$_4$/N-CNTs wrapped around GDL particles and present within the GDL pores.

To evaluate the success of GDL impregnation, cross sectional SEM images were obtained as well as EDX line scans (Figure 5). Mn$_3$O$_4$/N-CNTs are present both at the surface (Figure 5b) and ~100 μm (Figure 5c) into the microporous layer. As expected, there is a higher concentration of nanotubes present on the surface than deeper into the interior. Mn$_3$O$_4$ particles on the N-CNTs were used to track the relative amount of catalyst throughout the microporous layer via SEM EDX line scans. An example of a line scan is presented in Figure 5d and confirms that there are significant amounts of catalyst up to 35 μm from the surface of the GDL, after which the catalyst amount is significantly reduced.

Since impregnation of Mn$_3$O$_4$/N-CNT into the GDL occurs simultaneously with synthesis, the effect of electrode preparation was investigated electrochemically using as-purchased N-CNTs. Three preparation techniques were compared: spray coating, soaking, and vacuum filtration. The techniques were compared using half-cell LSV as well as full-cell discharge rate tests (Figure S4). For consistency, the catalyst loading was about the same for all N-CNT electrode samples (~1 ± 0.4 mg cm^{-2}). From Figure S4a, it is apparent that there is no significant difference between soaking and vacuum filtration techniques, while spray coating has the largest current at higher overpotentials. Furthermore, the spray coated sample has a relatively lower onset potential than the impregnated samples which is considered to be a result of higher accumulation of N-CNTs on the GDL surface. The lack of significant variation in the half-cell results can be attributed to oxygen saturation of the electrolyte. Since oxygen does not have to diffuse through the GDL and electrolyte to gain access to the catalysts, the half-cell performance is more dependent on surface catalyst loading.
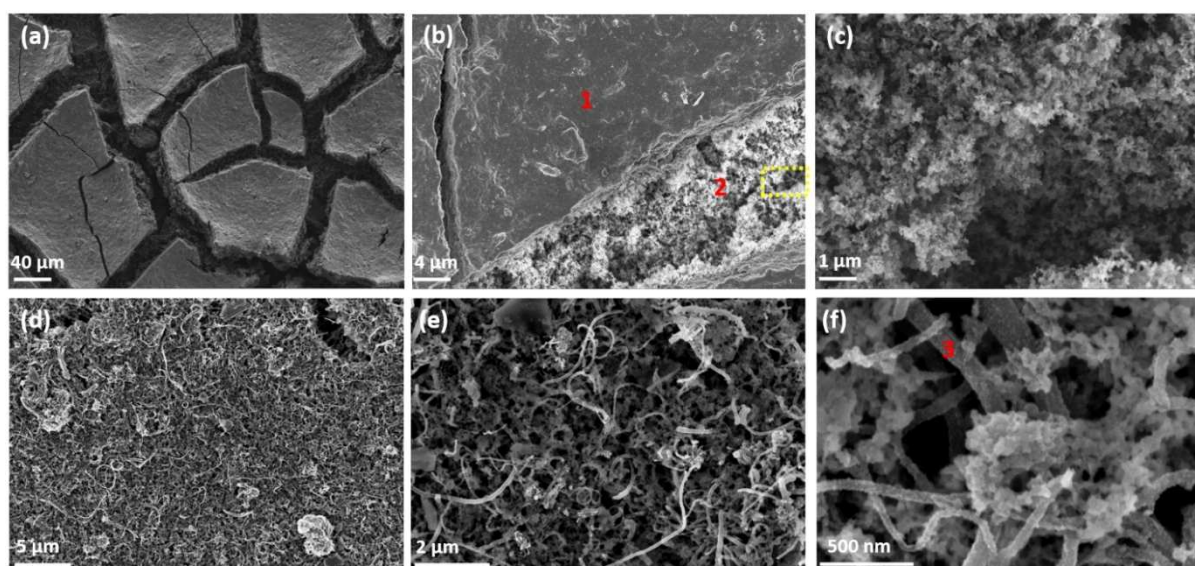

Figure 4. SEM secondary electron (SE) micrographs of the Mn$_3$O$_4$/GDL (a–c) and Mn$_3$O$_4$/N-CNT/GDL (d–f) sample surfaces. The Mn oxide film and GDL for Mn$_3$O$_4$/GDL can be seen in a) and b), while c) shows the GDL carbon particles from the region (yellow box) indicated in b) at higher magnification. The low magnification view of Mn$_3$O$_4$/N-CNT/GDL in d) shows catalysts across the GDL surface, while e) shows dispersion of Mn$_3$O$_4$/N-CNTs on and within GDL pores. The image in f) shows a high magnification view of Mn$_3$O$_4$/N-CNTs with visible Mn oxide particles on the nanotubes. Points used for EDX analysis are indicated by red numbers (b and f). Results for EDX point analysis are presented in Table 3.
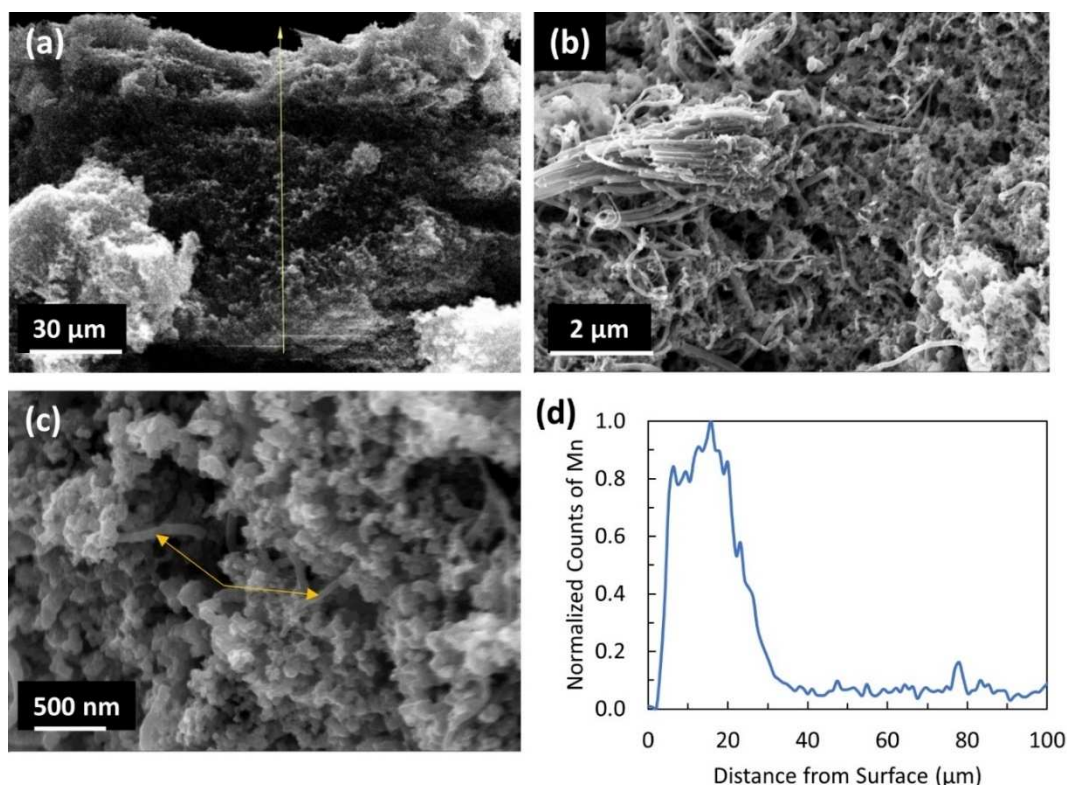
Figure 5. a) SEM SE micrograph from a cross section of the microporous layer used for EDX line scan in (d). b) SEM SE micrograph of Mn_3O_4/N-CNT/GDL sample surface. c) SEM SE micrograph of Mn_3O_4/N-CNT/GDL sample at a depth of ~100 μm into the GDL with arrows indicating the presence of nanotubes. d) Normalized Mn composition throughout the microporous layer from EDX line scan data. The Mn amount shown is relative to the maximum number of Mn counts obtained. Imaged samples were prepared by combined soaking and vacuum filtration.

The spray coating technique deposits more catalyst on the surface of the GDL than the other two techniques; compare Figure S5a and S5b (spray coated GDL samples) with S5c and S5d (soaked GDL samples). Infiltration, through either soaking or vacuum filtration, is expected to have a greater effect in full cell testing since oxygen needs to diffuse through the GDL layer to access the catalysts. This expectation is confirmed for soaked samples in Figure S4b. As the discharge current density is increased, the soaked sample experiences smaller decreases in discharge potential compared with the spray coated and vacuum filtered samples. Conversely, vacuum filtration appears to improve the performance at lower current densities, which suggests a higher accumulation of catalyst near the surface of the GDL. The difference between soaking and vacuum filtration is likely a result of the physical differences between the impregnation techniques. Soaking the GDL in the suspension during sonication allows catalysts to impregnate the GDL from both the surface (microporous layer) and back (macroporous layer), while vacuum filtration is directional and pulls the catalyst suspension from the microporous surface inwards. Therefore, there is a greater chance of the impregnated catalysts accumulating closer to the surface when using vacuum filtration. These tests were repeated for 10 soaked samples and 6 vacuum filtered samples, and the results were reproducible.

The preparation comparison of the N-CNT electrodes was used as a foundation for the work done with Mn_3O_4/N-CNT/GDL samples. To optimize the performance of the catalyst, a series of experiments was conducted to discover the effects of the concentration of hydroxide, the cation in the hydroxide used, the mass ratio of Mn to N-CNT, and the preparation method. Since the performance of the impregnated samples was best evaluated using full cell tests, battery discharge potentials were used to compare the effects of each variable and are shown in Figure 6. Figure 6a compares the Mn:N-CNT mass ratios in the suspensions (5:1, 7:1, 10:1). Although both the 5:1 and 10:1 samples reach a discharge potential of 1.21 V at 20 mA cm^{-2}, the 5:1 mass ratio was chosen as the better sample due to its relatively higher discharge potentials at lower current densities.

The morphologies of the 5:1 and 10:1 samples are shown in Figure S6. The surface of the electrode is comparable for both samples, showing many nanotubes with no distinct differences (Figure S6a and S6c). Higher magnification images (Figure S6b and S6d) show some N-CNTs decorated with larger particles for the 10:1 sample, while the 5:1 sample has many fine particles on virtually all N-CNTs. SEM EDX analysis confirms that the amount of Mn is higher for the 10:1 ratio sample; note the larger Mn:C ratio for the 10:1 sample in Table S1. There-fore, the slight differences in performance between samples
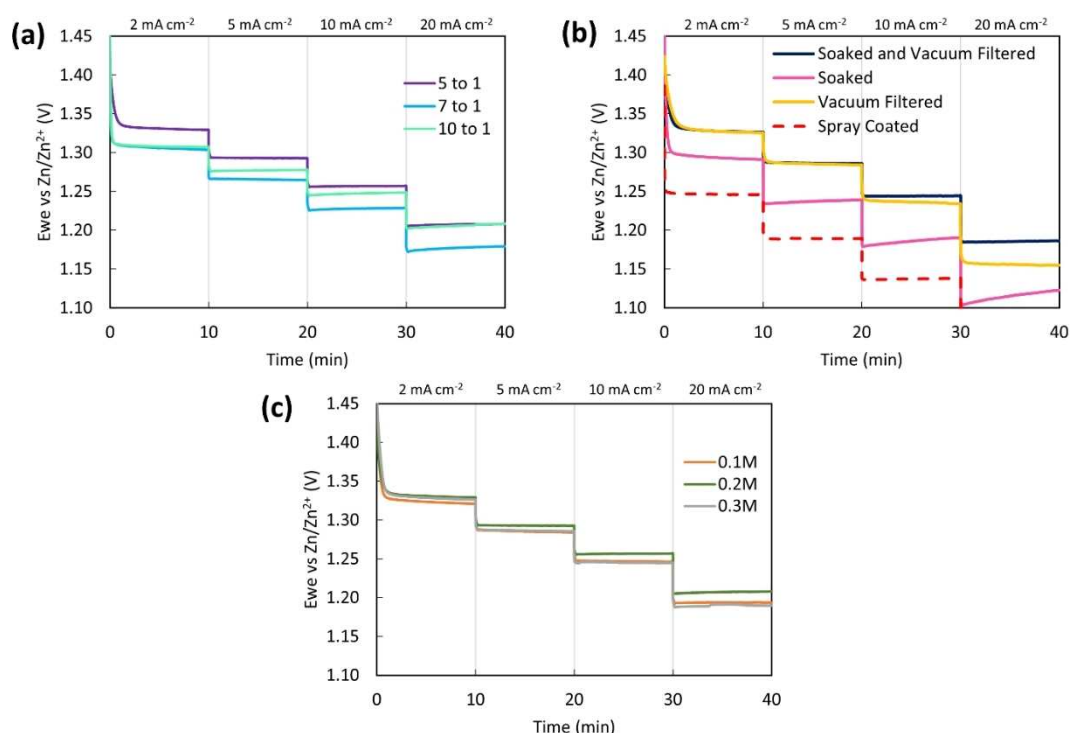
Figure 6. Full cell CV testing. a) Discharge rate comparison of different Mn : N-CNT ratios; b) discharge rate comparison of the different impregnation techniques for Mn_3O_4/N-CNT/GDL; c) discharge rate comparison of varying OH^- concentration in the catalyst precursor suspension.

with varying Mn : N-CNT ratios in suspension is thought to be related to the average Mn oxide particle size on the N-CNTs.

Figure 6b compares the preparation techniques in terms of discharge potential at different current densities. In addition to comparing the vacuum filtration and soaking methods of impregnation, a combined soaking and vacuum filtration method was explored. The soaked samples were prepared by soaking the GDL for 0.5 h to achieve a mass loading comparable to vacuum filtration. Soaked and vacuum filtered samples were prepared by 20 min of GDL soaking followed by 3 mL of suspension vacuum filtered through the GDL in order to maintain a comparable mass loading. All samples are also compared with spray coated Mn_3O_4/N-CNTs on GDL, which have the lowest discharge potentials (Figure 6b). Soaking, combined with vacuum filtering of the GDL with catalyst, improved the performance at higher current densities when compared with soaking or vacuum filtration alone. Moreover, soaking and vacuum filtration shows significant improvement when compared with conventional spray coating. This corroborates the results observed for N-CNTs. Using soaking and vacuum filtration together combines the benefits of the respective techniques. Vacuum filtration provides an adequate surface layer of the catalyst while better dispersion of the catalyst within the porosity of the GDL is achieved through soaking. As such, combined soaking and vacuum filtration was chosen as the optimal preparation method for impregnation.

Figure 6c compares the effect of OH^- concentration. Three concentrations of NaOH were investigated: 0.1 M, 0.2 M, and 0.3 M. There is very little difference in performance as the OH^- concentration is varied, with the samples prepared with 0.2 M

NaOH exhibiting slightly superior discharge potential at 20 mA cm^{-2}. 22 samples were synthesised using either NaOH or KOH. Table 4 shows the mean discharge potential and standard deviation (at 20 mA cm^{-2}) for the 22 samples prepared using both hydroxides. NaOH synthesized samples have slightly higher discharge potentials, with less variation between samples, for a lower average mass loading. The optimal fabrication process then includes a solution with 0.2 M NaOH and a 5:1 mass ratio of Mn to N-CNT, with 20 min of GDL soaking in the suspension followed by vacuum filtration with 3 mL of the suspension.

Using the optimized methodology, Mn_3O_4/N-CNT/GDL samples were prepared for half-cell and full-cell comparisons (Figure 7). Figure 7a shows that the ORR activity of the Mn_3O_4/N-CNT/GDL sample is superior to both N-CNT/GDL and Mn_3O_4/GDL which can be explained by the synergistic effect between Mn, N, and C. The addition of Mn_3O_4 active sites to the N active sites already present in the N-CNTs leads to higher catalytic activity; the N-CNTs also reduce the electronic resistance of the composite material.[10], [17][34] The onset potential for ORR in this work is defined as the measured potential at 10 mA cm^{-2}. The

Table 4. Comparison of hydroxide cation used for Mn_3O_4/N-CNT/GDL synthesis.

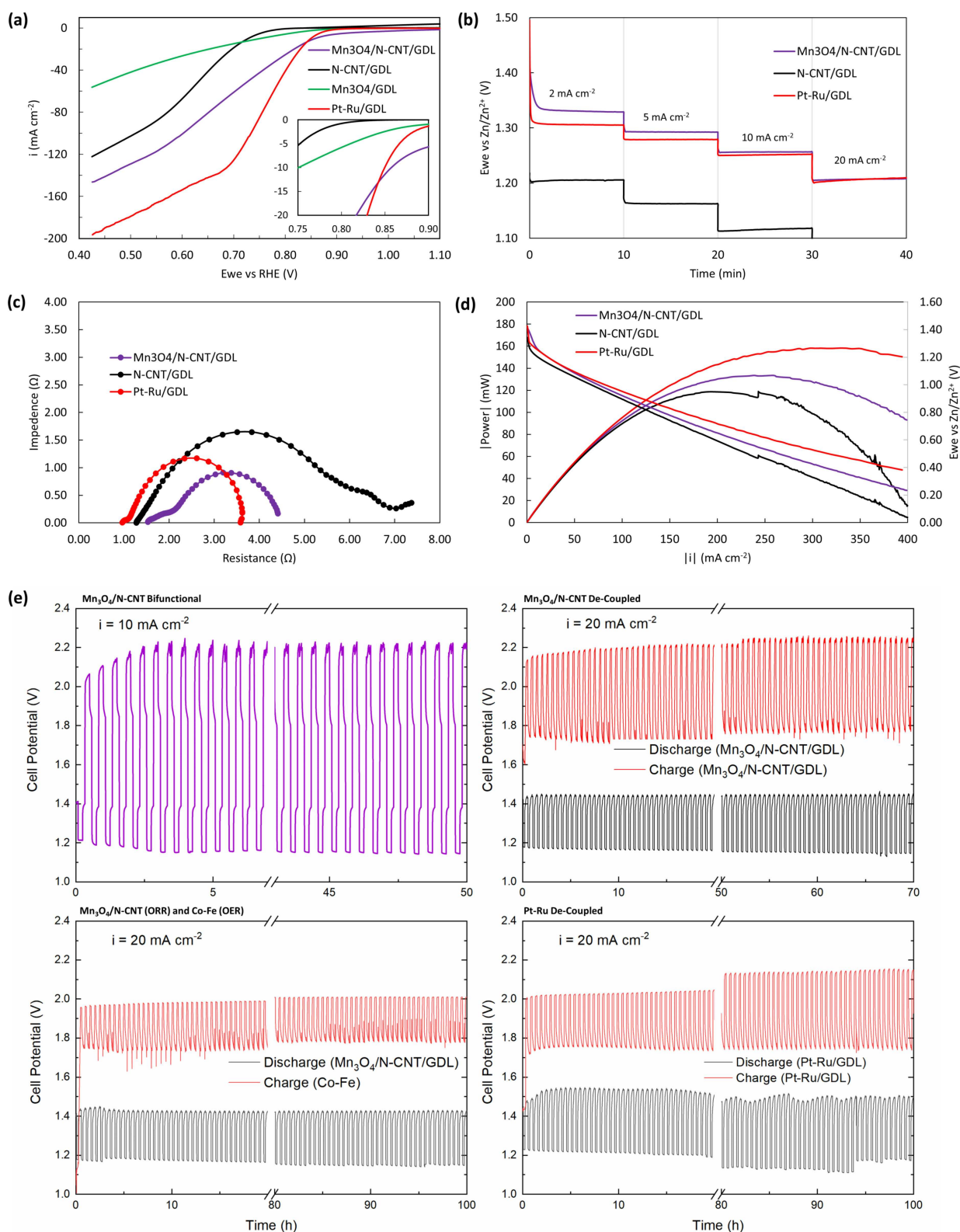|	Mean performance at 20 mA cm^{-2} (V)	Standard deviation (V)	Average mass loading (mg cm^{-2})
NaOH	1.19	0.019	1.89
KOH	1.15	0.039	2.75

Figure 7. Electrochemical and battery performance of Mn_3O_4/N-CNT/GDL: a) half-cell LSV comparison of various catalysts with Mn_3O_4/N-CNT/GDL; b) battery discharge rate comparison with Mn_3O_4/N-CNT/GDL; c) battery EIS spectra comparison with Mn_3O_4/N-CNT/GDL; d) power comparison with Mn_3O_4/N-CNT/GDL; e) bifunctional and de-coupled (tri-electrode) battery cycling in 6 M KOH + 0.25 M ZnO. Bifunctional cycling of Mn_3O_4/N-CNT/GDL was done at 10 mA cm^{-2} (100 cycles or 50 h). De-coupled cycling of Mn_3O_4/N-CNT/GDL as both ORR and OER electrodes (145 cycles or 72.5 h), de-coupled cycling of Mn_3O_4/N-CNT/GDL and Co−Fe on Ni foam as the ORR and OER electrodes, respectively (200 cycles or 100 h), and de-coupled cycling of Pt−Ru/GDL as both ORR and OER electrodes (200 cycles or 100 h) were conducted at 20 mA cm^{-2} in 6 M KOH + 0.25 M ZnO.

Mn_3O_4/N-CNT sample compares favourably with Pt—Ru (0.849 V vs RHE) with an onset potential of 0.854 V vs RHE. The competitive onset potential suggests strong ORR activity of the synthesized catalyst; however, Pt—Ru/GDL shows larger current at higher overpotentials. Mn_3O_4/N-CNT/GDL is primarily considered as an ORR catalyst in this work; however, its capability as an OER catalyst has been evaluated through LSV measurements (Figure S7). Clearly, the OER activity of Mn_3O_4/N-CNT is poor compared with Pt—Ru/GDL. The slight improvement in OER activity relative to Mn_3O_4/GDL is attributed to the presence of N-CNTs.

In full-cell battery discharge rate tests (Figure 7b), Mn_3O_4/N-CNT/GDL samples have discharge potentials greater than Pt—Ru at lower current densities and the same discharge potential of 1.21 V at 20 mA cm^{-2}, which essentially corroborates the LSV results in Figure 7a. The discharge rate results show better performance when compared with Mn_3O_4 particles on doped CNTs reported previously in the literature.[20,21] For instance, Li et al. reported a discharge potential of 1.20 at 2 mA cm^{-2} for Mn_3O_4/O-CNTs which is 140 mV lower than that of Mn_3O_4/N-CNT/GDL at the same current density (1.34 V).[21] Similarly, Mn_3O_4/N-CNT/GDL exhibits superior discharge potentials to Mn_3O_4 quantum dots supported on partially exfoliated N-CNTs at both 10 and 20 mA cm^{-2} (1.25 V and 1.21 V vs 1.21 V and 1.11 V).[20] The low electrical resistance of Mn_3O_4/N-CNT/GDL is confirmed by the EIS measurements (Figure 7c). Interfacial resistance can be estimated by the intercept of the Nyquist plot with the horizontal axis.[35,36] The similarity in interfacial resistance between the Mn_3O_4/N-CNT/GDL sample and the N-CNT/GDL sample confirms that the good conductivity of N-CNTs plays a significant role in reducing interfacial resistance. Charge transfer resistance can be used as a metric for catalytic activity and is evaluated by the size of the semi-circular region of the EIS Nyquist plot.[35,36] Mn_3O_4/N-CNT/GDL has the lowest charge transfer resistance when compared with both N-CNT/GDL and Pt—Ru/GDL. The Mn_3O_4/N-CNT/GDL sample achieves a maximum power of 133 mW cm^{-2} (Figure 7d). Pt—Ru still boasts a higher maximum power of approximately 150 mW cm^{-2}, although the Mn_3O_4/N-CNT/GDL samples have improved power compared with N-CNTs alone. From the polarization curves in Figure 7d, it is apparent that the performance of Mn_3O_4/N-CNT/GDL remains comparable to Pt—Ru until approximately 50 mA cm^{-2}. Therefore, the data suggests that improving the active surface area may not alter the behaviour of the electrochemical curves, but instead slightly shifts the power and polarization curves upwards. These results confirm that the higher active surface area achieved by impregnation improves the battery performance, although it may not directly affect the catalytic activity of Mn_3O_4/N-CNT/GDL.

Battery cycling tests were conducted in bifunctional (two-electrode) and de-coupled (tri-electrode with separate ORR and OER electrodes) configurations at 10 mA cm^{-2} and 20 mA cm^{-2}, respectively (Figure 7e). Bifunctional cycling of Mn_3O_4/N-CNT/GDL shows degradation of the catalyst under OER conditions, which was most significant during the first 5 cycles. The damage accumulated during the OER conditions over 100 cycles, leading to a reduction in the discharge potential by

approximately 50 mV (Figure 7e). It should be noted that the discharge potential decreases the most during the first 10 cycles, after which the potential is relatively stable. The initial efficiency was 60.1% and dropped to 51.7% after 100 cycles. Tri-electrode cycling with Mn_3O_4/N-CNT/GDL as both ORR and OER electrodes (de-coupled Mn_3O_4/N-CNT/GDL, Figure 7e) was conducted in order to confirm that degradation is due to the harsh oxidizing conditions during OER. Degradation was observed primarily for the OER electrode, while the ORR electrode was stable over 145 cycles with a decrease of less than 30 mV in discharge potential. Similar to the bifunctional cycling, the OER electrode was relatively stable after the initial degradation. An increase in charge potential was observed after 47 h due to O_2 bubble accumulation on the OER electrode surface. The bubbles increase the interfacial resistance at the electrode surface resulting in an increase in the potential. A similar phenomenon is observed for the ORR electrode during cycling of Pt—Ru/GDL (de-coupled Pt—Ru, Figure 7e). Oxygen bubbles accumulate on the ORR electrode surface which gradually increases the potential; the potential resets once the bubbles are expelled.

The stability during discharge is attributed to catalyst impregnation of the microporous layer. Once the electrolyte begins to flood the GDL during cycling, oxygen diffusing through the GDL maintains access to the catalysts as they are present throughout the microporous layer; as such, the three-phase boundary is preserved. In a typical GDL prepared by surface loading techniques, flooding of the electrode will result in a loss of the three-phase boundary as the solid catalyst is no longer readily accessible to oxygen. Oxygen is then forced to diffuse through the electrolyte to reach the catalyst layer which slows the oxygen reactions and decreases performance of the cell.[1,4]

The degradation of the air electrode during charging is believed to be due to Mn_3O_4 dissolution and re-deposition onto the electrode surface during cycling (Figure 8). Before cycling (Figure 8a and 8b), the nanotubes are clearly distributed across the surface of the GDL particles and in the pores of the microporous layer and Mn_3O_4 particles on the N-CNTs cause the surface of the nanotubes to appear rough. After OER cycling (Figure 8c and 8d), the nanotubes appear much smoother which is likely due to Mn_3O_4 loss. Since the ORR and OER electrodes of the tri-electrode configuration are submerged in the same electrolyte, Mn may dissolve from the OER electrode during charging and re-deposit on both the ORR and OER electrodes during discharging. Re-deposition on the electrode during ORR cycling is confirmed in Figure 8e and 8f, as Mn oxide sheets are visible on the GDL and around the Mn_3O_4/N-CNTs. Unlike the OER electrode, Mn_3O_4 particles are visible on the N-CNTs of the ORR electrode, indicated by the rougher nanotube surface. New deposits on the ORR electrode surface have little effect on discharge performance as the ORR reaction is not limited to the electrode surface due to impregnation of the GDL. Conversely, the OER reaction primarily occurs on the electrode surface and would be expected to suffer greater performance loss due to surface changes and the loss of Mn_3O_4 particles on the N-CNTs. New
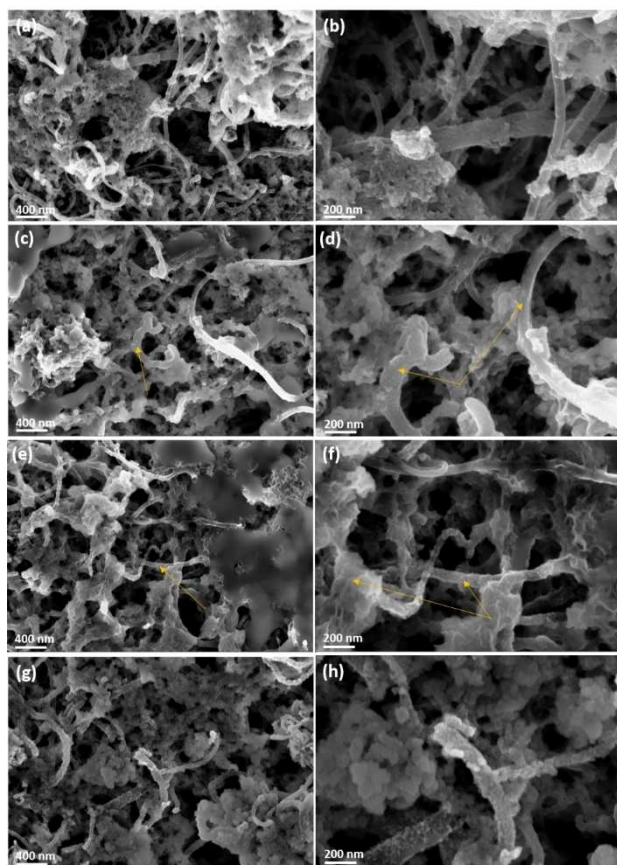
Figure 8. SEM SE micrographs of Mn$_3$O$_4$/N-CNT/GDL electrodes: a), b) before battery cycling; c), d) after OER cycling; e), f) after ORR cycling; g), h) after bifunctional cycling. Arrows are used to indicate regions of interest in d) and f) where Mn oxide deposition or dissolution are observed, respectively.

Mn oxide deposits and Mn dissolution limit the availability of surface Mn$_3$O$_4$/N-CNT catalysts for the OH$^-$ ions, thus slowing the kinetics of oxygen evolution.

The performance loss is more significant for the bifunctional electrode since it is exposed to both ORR and OER conditions (Figure 8g and 8h) and undergoes both Mn$_3$O$_4$ dissolution (charging) and re-deposition (discharging). Thus, the visible changes to the bifunctional electrode are less severe in comparison to the OER and ORR electrodes. However, the morphology of the particles on the N-CNT surface is altered when compared with the as-deposited sample (Figure 8a). Furthermore, thin Mn oxide sheets are visible on the GDL carbon particles after bifunctional cycling (Figure S8a and S8b), which confirms re-deposition similar to that of the ORR-exclusive electrode. Degradation of the Mn$_3$O$_4$ nanoparticles on the N-CNT surface reduces the activity of the catalyst towards both ORR and OER, while uncontrolled re-deposition of Mn$_3$O$_4$ onto the surface alters the active surface area for OER. Subjecting Mn$_3$O$_4$/N-CNT/GDL samples to both ORR and OER conditions will inevitably increase the rate at which the performance of the battery is lost. These findings agree with previous reports in the literature comparing two electrode and three electrode battery configurations.[1,37]

To achieve higher battery efficiency, tri-electrode cycling was conducted with Mn$_3$O$_4$/N-CNT/GDL and Co—Fe electrodeposited onto Ni-foam as the ORR and OER electrodes, respectively (Mn$_3$O$_4$/N-CNT/GDL and Co—Fe, Figure 7e). Electrodeposited Co—Fe was chosen as the OER electrode as it was shown in previous work to have good OER activity and durability during cycling.[27] The initial efficiency of the combined Mn$_3$O$_4$/N-CNT/GDL and Co—Fe tri-electrode battery was 61% when cycled at 20 mA cm^{-2}. After 200 cycles (100 h), the efficiency dropped only to 59%, boasting higher stability and cyclability than Mn$_3$O$_4$/N-CNT/GDL utilized as both de-coupled electrodes (51% efficiency after 150 cycles). A sudden jump in the ORR potential for the Mn$_3$O$_4$/N-CNT/GDL and Co—Fe battery was observed at 70 h and is due to accumulation and release of air bubbles under the horizontally positioned ORR electrode. Again, the ORR potential only decreases by 30 mV over 200 cycles, while the Co—Fe OER electrode potential increases by only 50 mV over 200 cycles. Additionally, the performance is superior to that of Pt—Ru/GDL tested in the same tri-electrode configuration (de-coupled Pt—Ru, Figure 7e). The ORR and OER electrodes both have superior durability after 200 cycles when compared with Pt—Ru, and the discharge-charge efficiency after cycling (59%) is 4% higher than that of Pt—Ru (55%). Battery discharge rate and battery cycling results also compare favourably with other transition metal and carbon-based ORR catalysts reported under similar testing conditions, particularly Mn$_3$O$_4$ catalysts supported on other CNT frameworks (Table S2).[1,20,21,25,38]

3. Conclusions

In summary, an ORR-active nanocomposite air electrode was synthesized in a one-pot process using Mn$_3$O$_4$-decorated N-CNTs and a simple impregnation method. The novel impregnation technique showed superior performance to other electrode preparation techniques in battery testing as a result of higher active surface area. The nanocomposite electrode displayed comparable performance to commercially used Pt—Ru catalysts and even superior performance to other Mn oxide catalysts supported on nanocarbon frameworks in terms of discharge potential and cyclability, while mitigating some of the adverse effects of flooding during cycling. The electrode also proved to be durable through battery cycling when used exclusively as an ORR electrode. Combining the impregnated electrode with a suitable OER-active catalyst (i.e., Co—Fe on Ni foam) in a physically decoupled tri-electrode battery configuration provided discharge-charge efficiencies superior to Pt—Ru. These results indicate that simple impregnation of appropriate nanocatalysts into the GDL may be a cost effective and reproducible means to preserve the three-phase boundary during flooding, while simultaneously providing good ORR performance and cycling of electrically rechargeable Zn-air batteries.

Experimental Section

Material Synthesis and Electrode Preparation

Using a synthesis procedure similar to that described by Li et al.,[21] 50 mg of multi-walled N-CNTs (30–50 nm OD and 1–2 μm length, purchased from MK Nano), 250 mg of $Mn(CH_3COO)_2 \cdot 4H_2O$, and 80 mg of NaOH were mixed with 10 mL of ethanol in a 30 mL glass flask under vigorous stirring at 800 RPM for 10 min. The suspension was then sonicated for 5 h, with 15 mL of ethanol and 1 mL of 5% Nafion added to the suspension at 4.5 h. Teflon coated porous carbon paper, sectioned into circular pieces 4.5 cm in diameter, was used as the GDL substrate and was soaked in the catalyst-precursor suspension for 20 minutes under sonication. The impregnated GDL substrates were removed and dried in air for 15 min. Once dry, 3 mL of the suspension was passed through each impregnated GDL piece by vacuum filtration (BOLA vacuum filter funnel, Finemech Inc.). The impregnated GDL pieces were then removed from the filter and annealed for 0.5 h at 300 °C, achieving composite GDL substrates impregnated with Mn_3O_4 decorated N-CNTs (denoted as Mn_3O_4/N-CNT/GDL) with a mass loading of approximately 2 mg cm^{-2}. The Mn oxide was identified as Mn_3O_4 through the characterization work, present in the Results and Discussion section. Composite GDL pieces impregnated with only Mn_3O_4 particles were also synthesized for comparison via the same procedure without the addition of N-CNTs (denoted Mn_3O_4/GDL).

To compare the effects of the impregnation techniques, GDL samples loaded with as-purchased N-CNTs (N-CNT/GDL) were prepared by spray coating, soaking for 30 min, and vacuum filtration. Spray coating of N-CNT/GDL samples was achieved by using an ink consisting of 50 mg N-CNTs, 1 mL DIW, 2 mL ethanol, and 0.1 mL of 5% Nafion. Soaked and vacuum filtered samples were prepared separately in a process similar to that described for Mn_3O_4/N-CNT/GDL samples. Pt—Ru samples (Pt—Ru/GDL) were also prepared, for baseline comparison, by spray coating GDL pieces with an identical ink made with 50 mg Pt—Ru/C powder (nominally 30% Pt and 15% Ru on carbon black, purchased from Alfa Aesar) instead of N-CNTs.

Materials Characterization

The composition and morphology of the samples were characterized using scanning electron microscopy (Tescan VEGA3 and Zeiss SEMs operated at 5–20 kV), transmission electron microscopy (JEOL JEM-ARM200CF TEM/STEM), and x-ray photoelectron spectroscopy (Krato AXIS Supra XPS, using a monochromatic Al—K$_\alpha$ X-ray source and a pass energy of 20 eV). Both SEM and TEM instruments were equipped with energy dispersive X-ray (EDX) spectrometers for composition analysis. SEM samples were prepared by attaching the composite GDL pieces to an Al stub using carbon tape. Cross-sectional SEM samples were prepared by freezing pieces of the impregnated or spray coated GDL in liquid N_2 followed by fracturing through the sample centre. The samples were then mounted using carbon tape onto an angled Al stub for imaging. For TEM samples, catalyst material was scraped off the surface of the GDL composite and dispersed in 1 mL of ethanol. The suspension was then dropped by pipette three times onto the carbon grids and left to dry in air. XPS samples were prepared by cutting the composite GDL into small pieces. No sputter clean was used during XPS due to the size of the Mn oxide particles. XPS spectra were calibrated using the C 1s peak at 284.4 eV.

Electrochemical Measurements

Electrochemical measurements were achieved using linear sweep voltammetry (LSV), cyclic voltammetry (CV), and electrical impedance spectroscopy (EIS). The techniques were conducted in 1 M oxygen saturated KOH using various potentiostats (Biologic SP300 and VSP-100) with a three-electrode configuration. The impregnated or spray coated GDL samples, Pt wire, and Hg/HgO (0.098 V vs. SHE) were used as the working electrode, counter electrode, and reference electrode, respectively. Pt—Ru/GDL was also used as the working electrode as a baseline material for comparison. The electrolyte was purged with pure O_2 gas and agitated by magnetic stirring. The reported current densities were normalized to the exposed surface area of the working electrode. The reported potentials were IR compensated ($R_u = 2$–$4\ \Omega$).

Battery Testing

Zn-air battery testing was conducted in both vertical and horizontal home-made cells using 6 M KOH mixed with 0.25 M ZnO as the electrolyte (Figure S1). The vertical cell had a two electrode configuration while the horizontal cell had a three electrode (tri-electrode) configuration with decoupled ORR and OER electrodes, as described in previous work .[39] The vertical cell consisted of an anode made from Zn sheet metal and catalyst loaded GDL (Mn_3O_4/N-CNT/GDL or N-CNT/GDL) as the air electrode. The horizontal cell utilized Zn sheet metal, Mn_3O_4/N-CNT impregnated GDL and electrodeposited Co—Fe on GDL as the anode, ORR electrode, and OER electrode, respectively. For comparison, Pt—Ru/GDL samples were also used as the air electrode for the vertical cell, and as both ORR and OER electrodes for the horizontal cell. Discharge and charge cycling were conducted at 10 mA cm^{-2} in the vertical cell and 20 mA cm^{-2} in the horizontal cell.

Conflict of Interest

The authors declare no conflict of interest.

[1] J. Fu, Z. P. Cano, M. G. Park, A. Yu, M. Fowler, Z. Chen, *Adv. Mater.* **2017**, *29*, 1604685.
[2] H. D. Yoo, E. Markevich, G. Salitra, D. Sharon, D. Aurbach, *Biochem. Pharmacol.* **2014**, *17*, 3, 110–121.
[3] M. Xiong, D. G. Ivey, *J. Electrochem. Soc.* **2017**, *164*, 6, A1012–A1021.
[4] E. Davari, D. G. Ivey, *Sustain. Energy Fuels* **2017**, *2*, 39–67.
[5] T. Reier, M. Oezaslan, P. Strasser, *ACS Catal.* **2012**, *2*, 8, 1765–1772.
[6] Y. J. Wang, N. Zhao, B. Fang, H. Li, X. T. Bi, H. Wang, *Chem. Rev.* **2015**, *115*, 9, 3433–3467.
[7] H. Osgood, S. V. Devaguptapu, H. Xu, J. Cho, G. Wu, *Nano Today* **2016**, *11*, 5, 601–625.
[8] A. R. Mainar, L. C. Colmenares, O. Leonet, F. Alcaide, J. J. Iruin, S. Weinberger, V. Hacker, E. Iruin, I. Urdanpilleta, J. A. Blazquez, *Electrochim. Acta* **2016**, *217*, 80–91.

[9] P. C. Li, C. C. Hu, T. H. You, P. Y. Chen, *Carbon* **2017**, *111*, 813–821.

[10] S. Zhao, L. Yan, H. Luo, W. Mustain, H. Xu, *Nano Energy* **2018**, *47*, February, 172–198.

[11] X. Zhang, X. Wang, Z. Xie, Z. Zhou, *Green Energy Environ.* **2016**, *1*, 1, 4–17.

[12] Q. Wang, K. Dastafkan, C. Zhao, *Curr. Opin. Electrochem.* **2018**, 1–8.

[13] A. L. Zhu, D. P. Wilkinson, X. Zhang, Y. Xing, A. G. Rozhin, S. A. Kulinich, *J. Energy Storage* **2016**, *8*, 35–50.

[14] G. Wu, A. Santandreu, W. Kellogg, S. Gupta, O. Ogoke, H. Zhang, H. L. Wang, L. Dai, *Nano Energy* **2016**, *29*, 83–110.

[15] Y. Wang, H. Fan, A. Ignaszak, L. Zhang, S. Shao, P. David, *Chem. Eng. J.* **2018**, *348*, 1, 416–437.

[16] H. Lin, D. Chen, C. Lu, C. Zhang, F. Qiu, S. Han, X. Zhuang, *Electrochim. Acta* **2018**, *266*, 17–26.

[17] N. T. Alvarez, V. N. Shanov, T. Ochmann, B. Ruff, Carbon Nanotube Fiber Doping. Elsevier 2013.

[18] Z. Chen, Z. Chen, D. Higgins, *Carbon* **2010**, *48*, 11, 3057–3065.

[19] Y. Gao, L. Wang, G. Li, Z. Xiao, Q. Wang, X. Zhang, *Int. J. Hydrogen Energy* **2018**, *43*, 16, 7893–7902.

[20] Z. Huang, X. Qin, X. Gu, G. Li, Y. Mu, N. Wang, K. Ithisuphalap, H. Wang, Z. Guo, Z. Shi, G. Wu, M. Shao, *ACS Appl. Mater. Interfaces* **2018**, *10*, 28, 23900–23909.

[21] L. Li, J. Yang, H. Yang, L. Zhang, J. Shao, W. Huang, B. Liu, X. Dong, *ACS Appl. Energy Mater.* **2018**, *1*, 963–969.

[22] J. Albero, H. Garcia, *J. Mol. Catal. A* **2014**, *408*, 296–309.

[23] C. Tang, M. M. Titirici, Q. Zhang, *J. Energy Chem.* **2017**, *26*, 6, 1077–1093.

[24] M. Inagaki, M. Toyoda, Y. Soneda, T. Morishita, *Carbon* **2018**, *132*, 104–140.

[25] P. Gu, M. Zheng, Q. Zhao, X. Xiao, H. Xue, H. Pang, *J. Mater. Chem. A* **2017**, *5*, 17, 7651–7666.

[26] S. Zhu, Z. Chen, B. Li, D. Higgins, H. Wang, H. Li, Z. Chen, *Electrochim. Acta* **2011**, *56*, 14, 5080–5084.

[27] M. Xiong, D. G. Ivey, *Electrochem. Commun.* **2017**, *75*, 73–77.

[28] G. A. M. Ali, M. M. Yusoff, Y. H. Ng, H. N. Lim, K. F. Chong, *Curr. Appl. Phys.* **2015**, *15*, 10, 1143–1147.

[29] A. Sumboja, F. Wei, T. Goh, B. Li, D. Geng, *ChemPlusChem* **2015**, *80*, December.

[30] M. Chigane, M. Ishikawa, *J. Electrochem. Soc.* **2000**, *147*, 6, 2246–2251.

[31] Y. Gorlin, B. Lassalle-kaiser, J. D. Benck, S. Gul, S. M. Webb, V. K. Yachandra, J. Yano, T. F. Jaramillo, *J. Am. Chem. Soc.* **2013**, *135*, 8525–8534.

[32] M. P. Clark, T. Muneshwar, M. Xiong, K. Cadien, D. G. Ivey, *ACS Nano* **2018**, *2*, 267–277.

[33] M. Chigane, M. Ishikawa, M. Izaki, *J. Electrochem. Soc.* **2001**, *148*, 7, 96–101.

[34] Z. Yang, H. Nie, X. Chen, X. Chen, S. Huang, *J. Power Sources* **2013**, *236*, 238–249.

[35] G. M. Ehrlich, Handbook Of Batteries. **2002**.

[36] L. Faulkner, A. Bard, Electrochemical Methods, Second Edi. **2001**.

[37] M. Xiong, M. P. Clark, M. Labbe, D. G. Ivey, *J. Power Sources* **2018**, *393*, May, 108–118.

[38] X. Chen, Z. Zhou, H. E. Karahan, Q. Shao, L. Wei, Y. Chen, *Small* **2018**, *1801929*, 1–29.

[39] M. Xiong, M. P. Clark, M. Labbe, D. G. Ivey, *J. Power Sources* **2018**, *393*, May, 108–118.